Al/Al_2O_3 MICROCHANNEL PLASMA CHEMICAL REACTOR FOR OZONE SYNTHESIS

BY

MIN HWAN KIM

THESIS

Submitted in partial fulfillment of the requirements
for the degree of Master of Science in Nuclear, Plasma, and Radiological Engineering
in the Graduate College of the
University of Illinois at Urbana-Champaign, 2013

Urbana, Illinois

Master's Committee:
Professor J. Gary Eden, Director of Research
Professor David N. Ruzic

Abstract

Ozone is produced efficiently in arrays of linear microplasmas at low temperatures and generated within alumina (Al_2O_3) microchannels. The array of microchannels device is fabricated from aluminum foil by chemical processing and mechanical ablation with photolithographic steps. Channels with 3 cm in length and 250 μm in width at the aperture of the channel produce spatially-uniform glow discharges in O_2 or dry air feedstock gases at a pressures of 1 atmosphere and flow rates of 0.25 – 2.5 standard liters per minute (slm). Several devices and array structures, including Al/Al_2O_3 or glass channels, also have been fabricated and tested. Efficiencies and O_3 concentrations surpassing 104 g/kWh and 17 g/Nm^3, respectively, have been measured, and arrays as large as 24 microchannels have been tested in this thesis. The results presented here suggest a new approach to plasmachemical reactors, one in which "massively parallel" processing of one or more gases in non-streamer glow discharges efficiently produces products of commercial value in thousands of microchannels fabricated in recyclable and inexpensive materials. Reductions of at least an order of magnitude in the weight and volume of microplasma-based O_3 reactors, relative to conventional dielectric barrier discharge technology, appear to be feasible.

Thanks to God for my Redeemer

Acknowledgements

First of all, I would like to thank to everyone at the Laboratory for Optical Physics and Engineering (LOPE) at the University of Illinois at Urbana-Champaign, especially Dr. Cho, Tom Houlahan, Darby Hewitt, Taegon Oh, Peter Sun, and undergraduate students for their assistance on my research. In addition, thanks for academic advisor Professor David Ruzic, and also I would like to give very special thanks to my advisors Professor J. Gary Eden and Professor Sung-Jin Park who let me work and learn at the laboratory and gave great support, guidance, and advice throughout both my undergraduate and graduate research.

Table of Contents

Chapter 1 – Introduction

Ozone is a strong oxidizing agent widely used for disinfecting and chemical processing [4-7]. The lethality of O_3 with regard to protozoan parasites, including *cryptosporidium*, and bacteria such as *Escherichia coli* [6,7], makes it a particularly effective disinfectant. Algae coagulation removal and deodorization, decoloration, and disinfection of wastewater by O_3 have been reported, and the extension of food storage lifetimes [4-7] is a major factor driving the growth of ozone generation capacity worldwide. Various configurations and technologies based on atmospheric-pressure plasmas for ozone synthesis have been extensively investigated, including the corona discharge (CD), the dielectric barrier discharge (DBD), microhollow cathode discharges (MHCD), and surface discharges (SD) [8-13]. However, the cost and complexity of these technologies present a significant barrier to the broad adoption of ozonation for the disinfection of municipal water supplies.

A new approach to the plasmachemical production of ozone and other molecules, radicals, and excited atoms or ions of commercial or environmental value is reported here. In particular, microchannel plasmas produced in either air or oxygen (as the feedstock gas) at atmospheric pressure are spatially-uniform glows along the entire 3 cm length of the channels. Efficiencies for ozone generation as high as 104 g/kWh and O_3 concentrations up to 17 g/Nm^3 have been realized in an array of 12 microchannels with an oxygen flow rate of 0.5 slm. Also, a greater rate of ozone production can be achieved by increasing the number of microchannels in the array. This scalability makes possible the construction of larger reactors based on microplasma technology, where the desired throughput determines the overall size of the system. The microchannel plasma generators with

optimized microchannel/electrode geometries will at least match the efficiency of large conventional DBD reactors in producing ozone, and will do so while reducing the reactor volume by at least an order of magnitude.

Chapter 2 – Background

2.1. Microplasma

Microplasmas are defined as weakly ionized, low temperature and non-equilibrium plasmas confined to a cavity or a channel with characteristic dimensions of 1 μm to 1 mm. These plasmas can operate up to the pressures of 1.5 atm (and beyond) and specific power loadings of 10^4 to 10^6 W/cm^3 [2]. The range in electron density that is typically available is 10^{13}~10^{16} cm^{-3}, and the cavity characteristic dimension is generally a few hundred microns (cf. Figure 1). Also, given the magnitude of the electron density (n_e) in microplasmas, the Debye length (λ_D) and plasma frequency (ω_p), given a characteristic dimension (d), are expressed as:

$$\lambda_D = \sqrt{\left(\frac{\varepsilon_0 T_e}{e^2 n_e}\right)} \tag{2.1}$$

$$and \quad \omega_{pe} = \sqrt{\left(\frac{e^2 n_e}{m\varepsilon_0}\right)} \tag{2.2}$$

where e is the charge and m is mass of an electron.

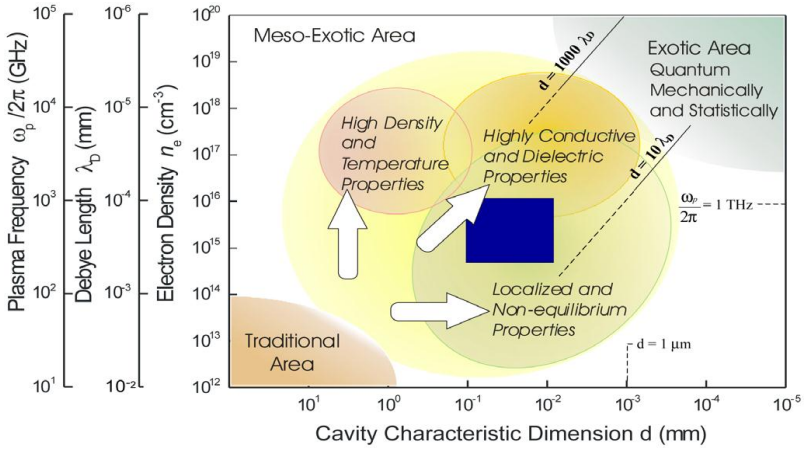

Figure 1. Plasma parameter map identifying several regions, broadly classified in terms of the relationship between the microcavity characteristic dimension (d) and electron density (n_e), Debye length (λ_D), or plasma frequency ($\omega_p/2\pi$) [2].

2.2. Electrical Breakdown of Gases

Paschen's law, which expresses the breakdown voltage for a discharge as a function of the gas pressure *p* and the gap length *d*, is an important relationship for both microplasmas and macroscopic plasma systems.

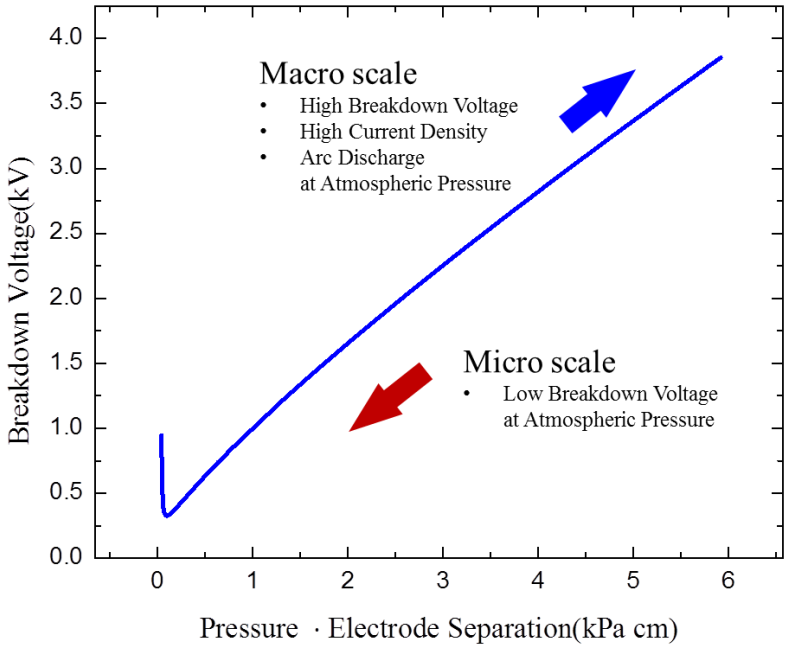

Figure 2. General Paschen breakdown curve for air.

Since macroscale discharges in atmospheric pressure gases require voltages of several kV, plasma breakdown and the transition from the glow to the arc mode occurs quickly and is difficult to control (Figure 2). However, as the characteristic dimension of the discharge is decreased to less than ~ 1 mm, the breakdown voltage is reduced and operation of the plasma in a glow mode is observed. Also, the electric field strength can be controlled by varying the electrode configuration or the separation between the electrodes.

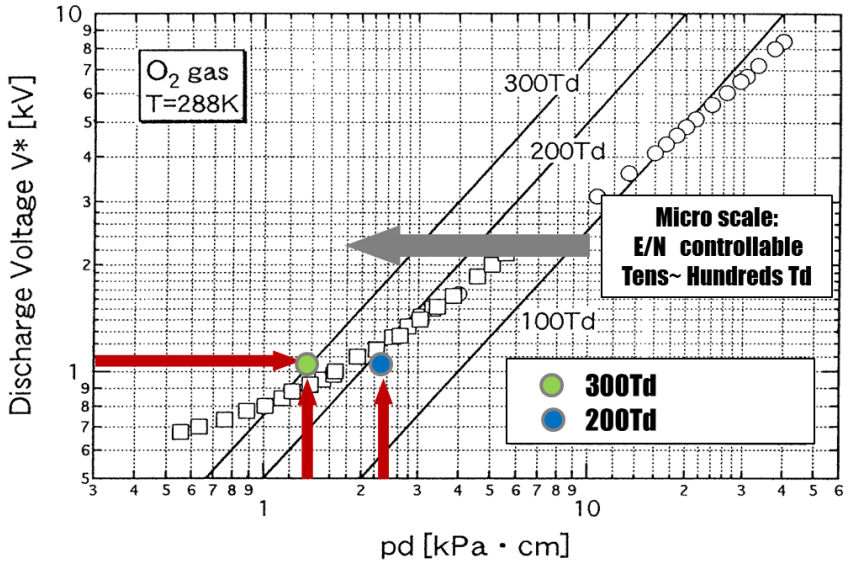

Figure 3. Discharge voltage versus *pd* values in different E/N for oxygen gas at 288 K. This figure is after Ref [14].

As an example, Figure 3 shows the discharge (operating) voltage V as a function of the *pd* product for plasmas produced in oxygen at 288 K[14]. The solid lines represent fixed values of E/N, where E is the electric field strength and N is the gas number density, which has units of Td (Townsends) and where 1 Td = 10^{-17} V-cm^2. At a fixed discharge voltage of 1-1.5 kV and a pressure of 1 atm, the electric field strength and, therefore, E/N can be modified significantly by changing the electrode separation.

2.3. Ozone

In 1987, Eliasson and co-workers published a paper, entitled "Ozone synthesis from oxygen in dielectric barrier discharges", which gives a comprehensive model for ozone generation in a dielectric barrer discharge (DBD) system.[9] On the basis of this work as well as Refs. 11 and 12, the following two mechanisms have been

identified as being those primarily responsible for the generation of ozone in low temperature plasmas:

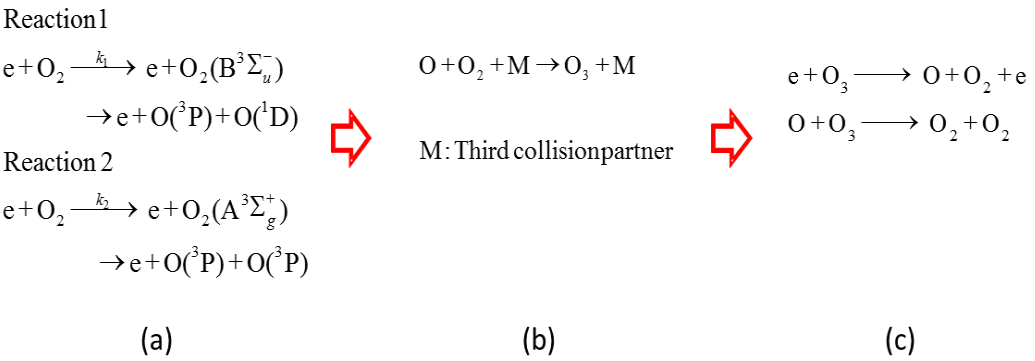

Figure 4. Most prominent ozone-forming reactions in a dielectric barrier discharge system: (a) Electronic dissociation of oxygen molecule; (b) Three body collision reaction to make an ozone molecule with an assistant third collision partner, M; (c) Recombination of electron or oxygen radical and ozone molecule to generate oxygen molecule.

The rate constant for the dissociation of the oxygen molecule by electron impact is a function of E/N, and the recombination reaction rate constant is a function of gas temperature. A more detailed discussion regarding ozone formation mechanisms will be given in Chapter 4.

Chapter 3 - Experimental Setup

3.1. Fabrication

Arrays of microchannel devices with a total thickness of less than 1 mm have been designed and fabricated in aluminum foil or glass substrates. One electrode in the device is prepared in aluminum foil covered by an Al_2O_3 dielectric layer. This aluminum electrode was prepared by electrochemical oxidation (an anodization process) so as to leave a buried aluminum electrode within nanoporous structured alumina (Al/Al_2O_3) (Figure 5). Another electrode was prepared in soda lime glass, and the glass substrates were coated with 100 nm of indium tin oxide (ITO) which is a transparent and electrically conductive material.

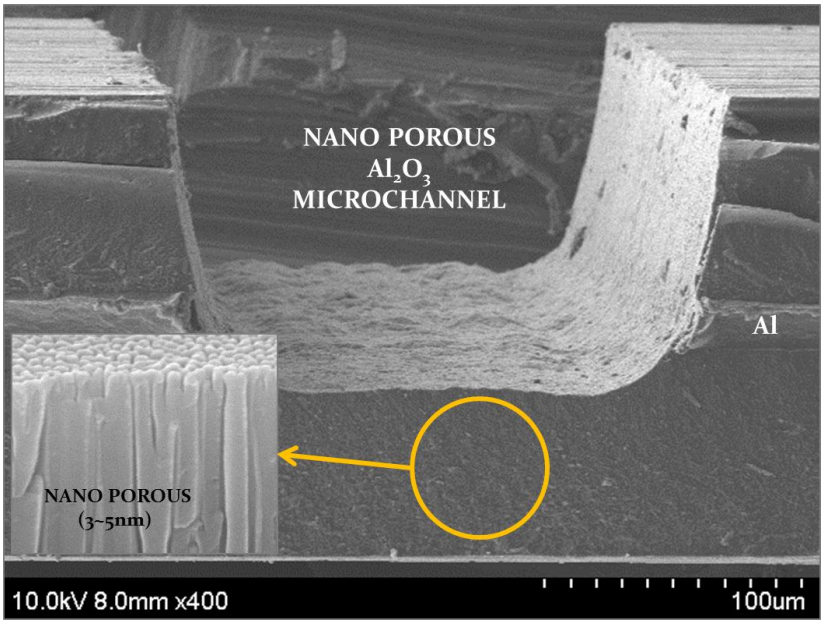

Figure 5. Scanning electron micrograph (SEM) of a trapezoidal trench in nanoporous Al_2O_3, viewed slightly off-axis. The Al electrodes buried in the alumina wall of the channel can be seen, and a magnified view of the nanoporous Al_2O_3 dielectric is at lower left. Note that, for this specific device, the Al electrode does not lie beneath the microchannel as was the case in Figs. 7(b) and 7(c).

In order to form microchannels in either the Al/Al_2O_3 or glass electrodes, ultraviolet (UV) curable polymer was deposited onto the surface of the electrodes which were then heated at ~40 ^oC. Then, a patterned polydimethylsiloxane (PDMS) stamp was evenly pressed into this layer of UV curable polymer, and was subsequently cured with strong UV light. After that, the PDMS stamp was removed, leaving the UV polymer behind with the desired microchannel array pattern for producing microchannels. The patterned polymer was then mechanically etched by a pressurized stream of microscale abrasive powder, thereby forming the microchannel pattern in the glass or oxidized aluminum substrate. The other side of the device was formed in a similar manner and using the same materials- oxidized aluminum or ITO coated glass. The final step in the device fabrication process was assembling the prepared electrodes by bonding the two pieces together with a hermetic sealant.

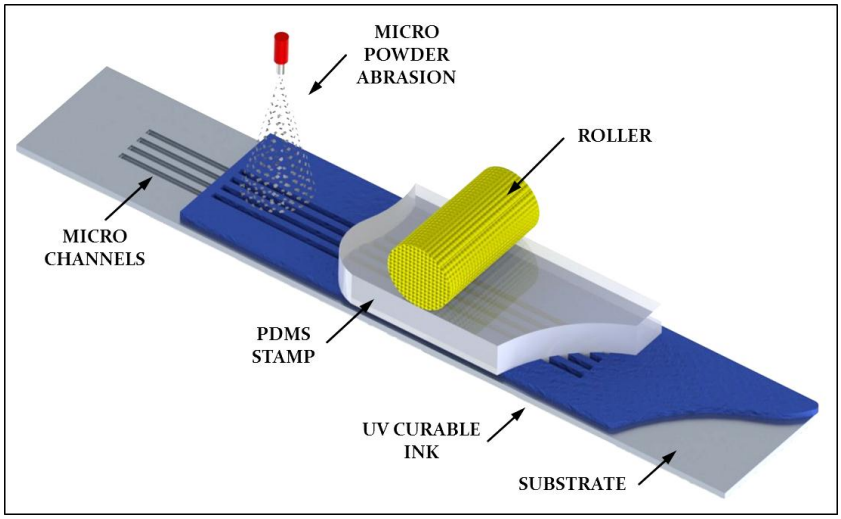

Figure 6. Composite illustration (not to scale) of the processes used to fabricate microchannel arrays in glass or nanoporous alumina (Al_2O_3) substrates

In this thesis, the cross-sectional profile of every microchannel is that of a half

ellipsoid. However, the surfaces of each channel can be controlled by the processing conditions or the selection of specific substrate materials. The dimensions typical of the channels for the research described here were 250 ± 10 µm for the channel width (at the channel aperture), 150 ± 10 µm in depth, and 30 mm in length (Figure 7). The volume of an individual channel was calculated to be 7.1 ± 0.1 mm^3.

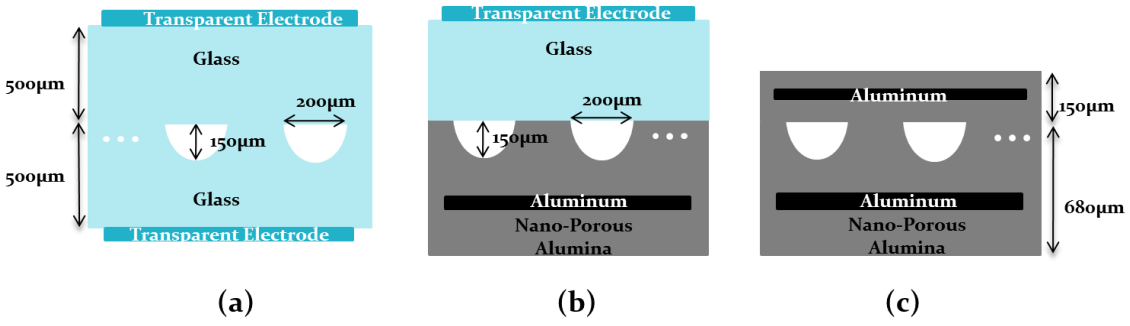

Figure 7. Cross-sectional diagrams of the DBD microchannel plasma device designs examined in the present experiments: (a) Double glass wafer structure; (b) A hybrid glass/nanoporous alumina structure in which a planar Al electrode is buried in Al_2O_3; (c) A fully Al/Al_2O_3 design incorporating two Al electrodes. All of these devices are hermetically sealed and the cavity cross section can be varied from parabolic to trapezoidal (i.e., linear taper of the sidewalls).

3.2. Experimental Setup

Experiments were conducted using pure oxygen and compressed air gas with flow rates from 0.1 slm to 1.5 slm. The produced ozone concentration was measured with a calibrated ozone monitor (Teledyne Model 454(H)) which had a stated precision less than 0.01 wt. % for O_3 gas. The device was driven with a 20 kHz sinusoidal voltage having a magnitude up to 2 kV (RMS). Device voltage and currents were monitored by a digital oscilloscope (Agilent DSO5054A) with high voltage and current proves (Tektronix P6015A and Pearson 2877, respectively). Figure 8 is a simple diagram of the measurement instruments and the inset is a cutaway view of only two channels of a microchannel array device.

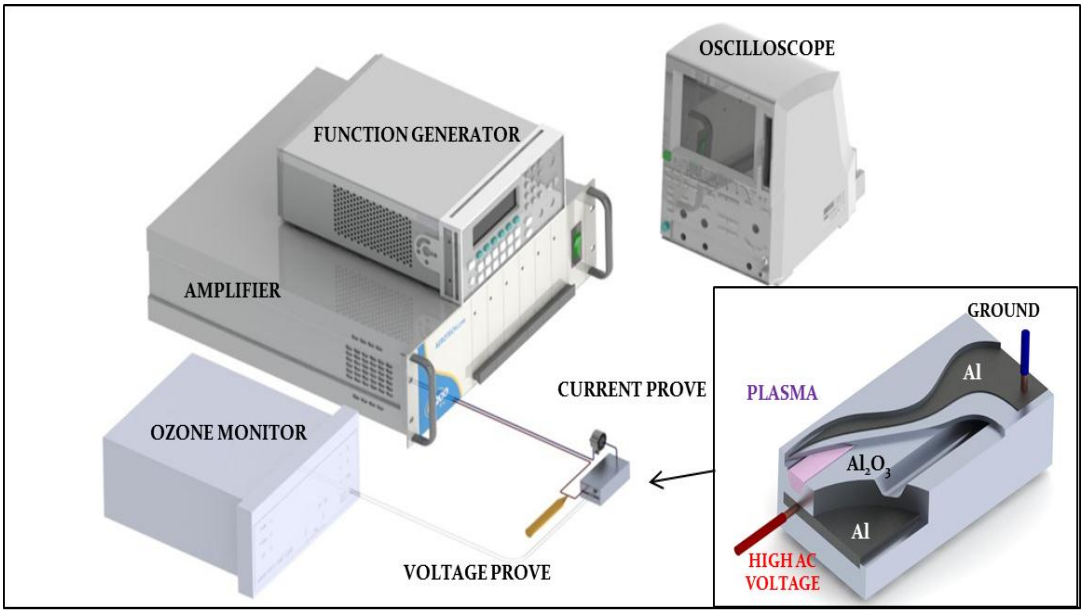

Figure 8. Simple testing setup image to operate device and simplified discharging image.

3.3. Data Acquisition Procedures

Figure 9 is a photograph, recorded in plan view, of a 12 microchannel reactor representative of those introduced into the hybrid device of Figure 7(b). Also, an image of the end-on fluorescence emanating from a portion of an array of Al/Al_2O_3 microchannels is shown in Figure 10. Recorded with a telescope and a charge-coupled device (CCD) camera, the image demonstrates that the fluorescence produced in the microchannels is steamer-free. Still higher magnification images of the axial fluorescence produced by the microchannels were obtained with an improved imaging arrangement involving an intensified, gated CCD (ICCD) detector, and Figure 11 presents false color images of the spatially-resolved emission intensity observed for a single channel with linear taper sidewalls.

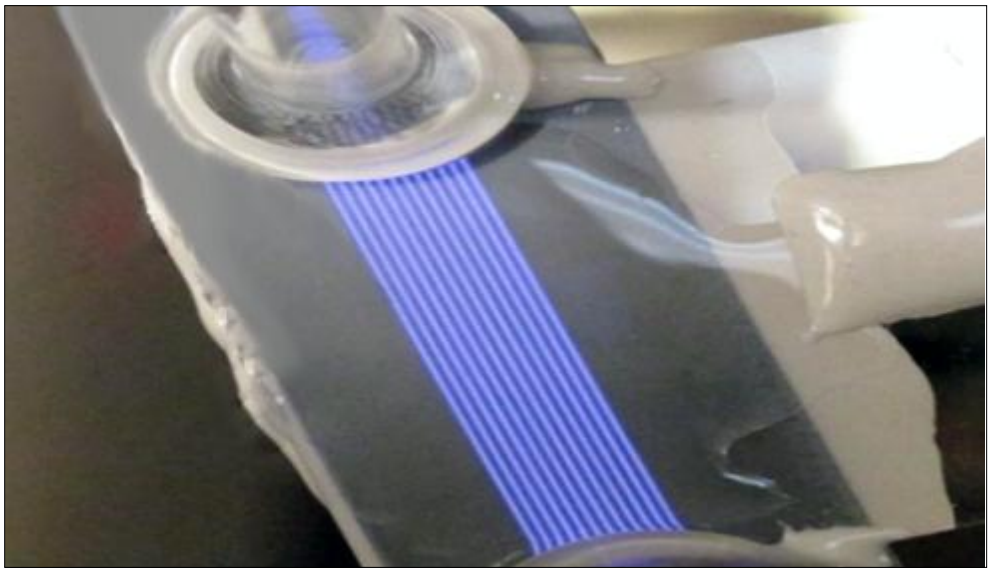

Figure 9. Photograph in plan view, showing the operation of a hybrid, 12 channel microplasma reactor operating in 1 atm of air.

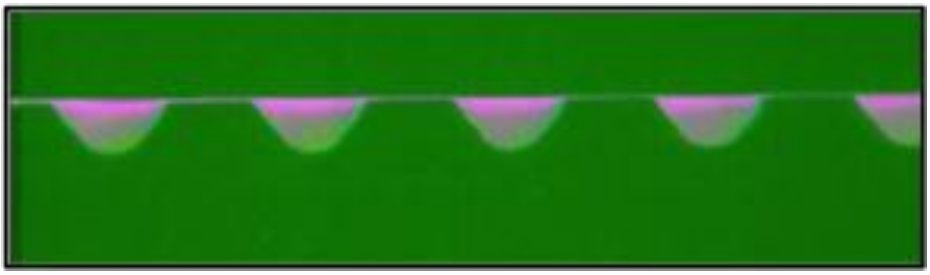

Figure 10. Optical micrograph (obtained with a CCD camera and a telescope) of the end-on fluorescence produced in 1 bar O_2 by an array of Al/Al_2O_3 microchannel plasmas.

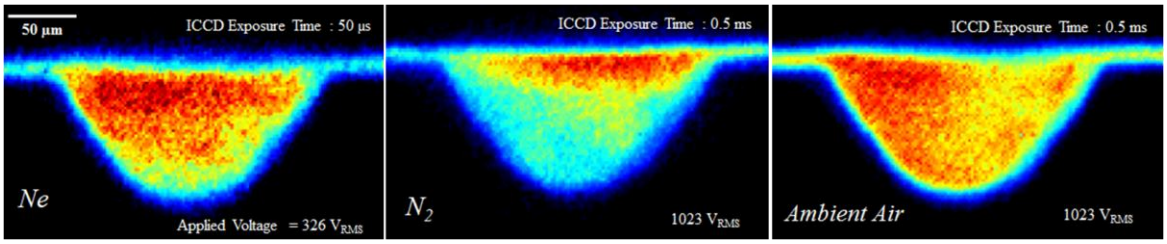

Figure 11. False color images of the spatially-resolved visible emission intensity produced end-on by microchannel plasmas in Ne, N_2, and ambient air. All of these data were acquired with an ICCD and telescope when driving the plasma with a 20 kHz sinusoidal voltage of 326 V (RMS) for Ne and 1023 V for both N_2 and air. The images were captured with ICCD gate widths of 50 µs (Ne) and 0.5 ms for N_2 and air.

Recorded at 1 atmosphere of Ne, N_2, or ambient (laboratory) air with sinusoidal (20 kHz) driving RMS voltages of 326 V, 1023 V, and 1023 V, respectively, the images of Figure 11 show reasonably uniform power deposition in the channel for Ne but a clear inability of the plasma to utilize the lowest portion of the channel where numerical simulations show the electrical field strength inside the channel to be at its weakest. In the case of ambient air, visible emission intensity from the plasma is not uniform but the plasma does occupy virtually the entire channel. Contrasting this behavior with the markedly different result for N_2 alone provides a vivid illustration of the ability of these microchannels to confine low temperature plasma and deliver power to an attaching gas at atmospheric pressure.

Chapter 4 - Results and Discussion

4.1. Comparative Performance of Glass, Al/Al_2O_3, and Hybrid Channel Devices

Figure 12 and Figure 13 show the operating voltage and current recorded for three devices having different electrode configurations. Figure 12 shows voltage and current waveforms with respect to time over one cycle of the driving voltage waveform while plasma was forming in channels of the devices. The devices were driven by a 20 kHz sinusoidal voltage with a peak-to-peak magnitude of 1.5 – 3.2 kV, and the data shown were obtained for a mass flow rate of 0.5 slm of oxygen gas flowing through 12 microchannels. It should be noted that the discharge currents for individual devices are clearly different from each other. In particular, the numbers of discharge current spikes occurring between 0 and 10 μs in the positive half cycle were significantly higher for Al/Al_2O_3 devices as compared to those for the two other devices. This result is attributable to the high power loading of the plasma in the case of the aluminum/alumina structure (which has a thinner dielectric) so strong excitation of the discharge gases is expected. For the same reason, the breakdown voltage of the devices was lower in the Al/Al_2O_3 devices, relative to the hybrid or glass structures, by a factor of 2.

Due to the robustness of the Al_2O_3 dielectric, no degradation of the device wall is observed after operating the devices for 1000 hours. It should also be mentioned that larger displacement currents were observed for the alumina devices because of their increased capacitance relative to the glass or hybrid structures.

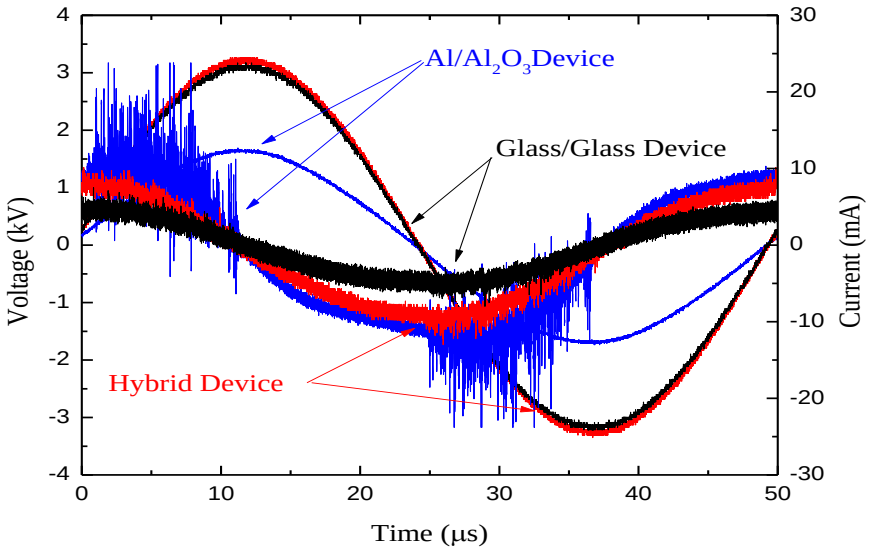

Figure 12. Voltage and current waveforms for the three microchannel device structures of Fig. 7. The waveforms were recorded for arrays comprising 12 microchannels and an O_2 flow rate of 0.5 slm.

As shown in Figure 13, the glass and hybrid devices required higher operating voltages than those for the Al/Al_2O_3 device because the distances between the two electrodes for the glass and hybrid devices were approximately 420 μm and 630 μm, respectively, as compared to the 370 ±10 μm for the Al/Al_2O_3 devices.

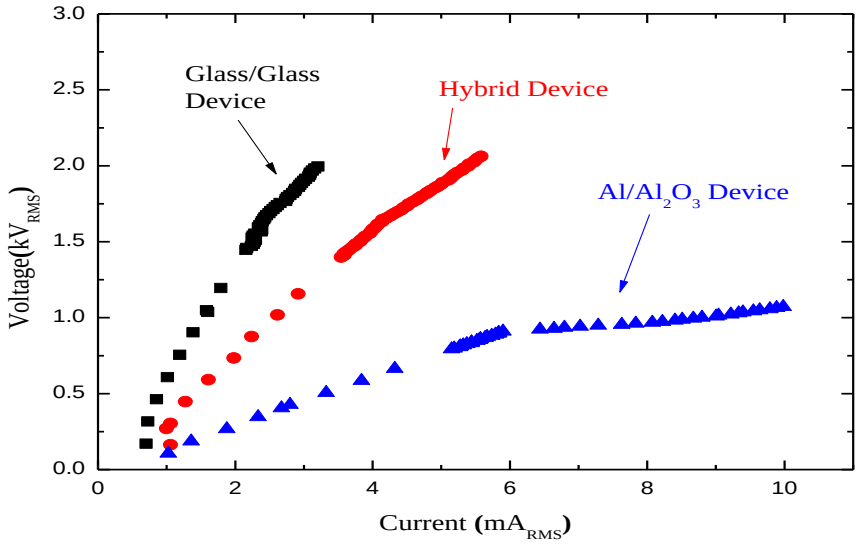

Figure 13. Voltage-current (V-I) characteristics for the three classes of microchannel designs examined in this work. All data were obtained for an O_2 flow rate of 0.5 slm and the measurements represent RMS values. The dashed line corresponds to a plasma impedance of ~41 kΩ.

The breakdown voltage for the glass and hybrid devices were measured to be approximately 1.5 kV (RMS), while the breakdown voltage for the Al/Al_2O_3 device was 950 V (RMS). After breakdown, the discharge currents for all the devices varied linearly with the driving voltage.

Figure 14 shows measurements of the ozone production rate (expressed in g/hr) versus the total measured current, which includes both the displacement and discharge current components. The ozone production rate can be calculated from Eq. (4.1) by multiplying C (the O_3 concentration in g/Nm^3) and Q (the gas flow rate, expressed in slm):

$$O_3 \text{ Production Rate} = \text{Concentration}\left(\frac{g}{m^3}\right) \times \text{Flow Rate}\left(\frac{m^3}{hr}\right). \qquad (4.1)$$

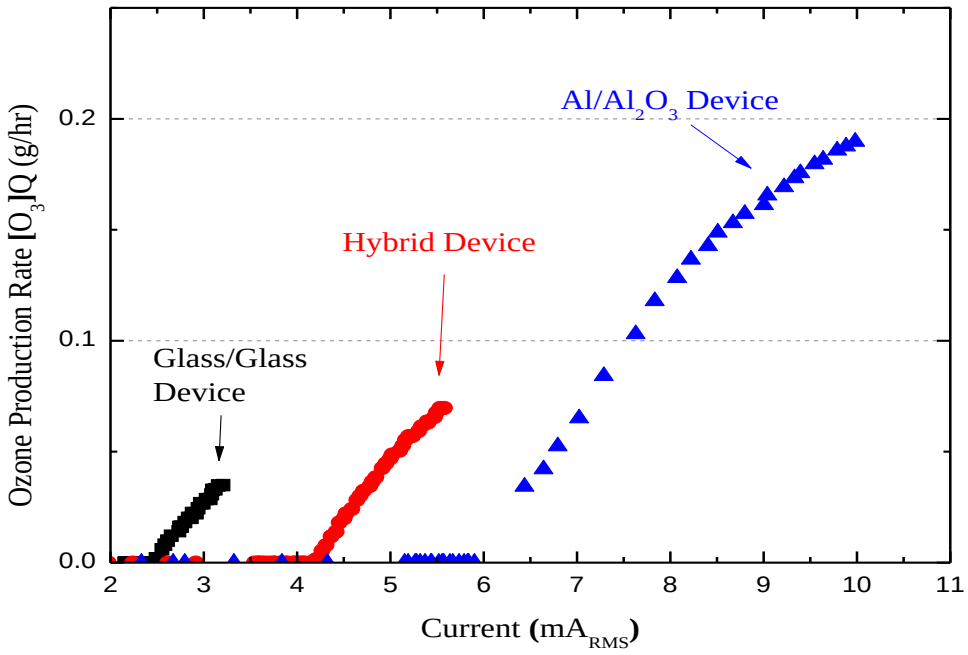

Figure 14. Dependence of ozone production rate on the current delivered to a 12 channel array. Data are given for glass/glass, hybrid, and Al/Al_2O_3 device designs, and the O_2 flow rate for all measurements was 0.5 slm.

The ozone production rate measured from the Al/Al_2O_3 device was the highest of the three devices, and it was up to 4 times higher than that for the glass device, depending on the discharge current and voltage used to drive the device. The ozone production efficiency can be calculated from the equation:

$$\eta = \frac{O_3\ Production\ Rate(g/hr)}{Discharge\ Power(W)} \ . \qquad (4.2)$$

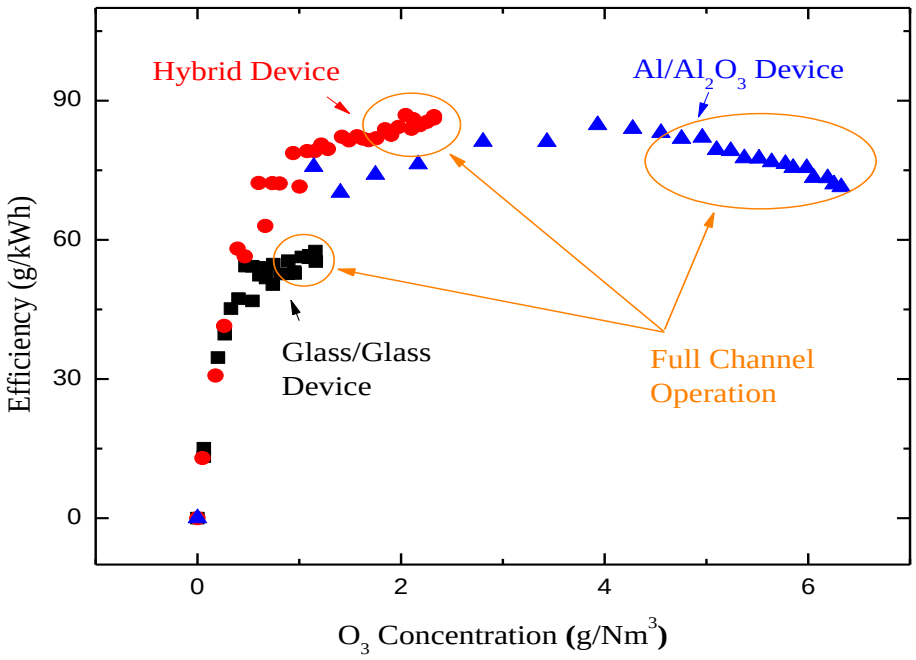

Figure 15. Variation of the O_3 generation efficiency η with the ozone concentration (C) for an O_2 gas flow rate of 0.5 slm. Data are given for the three microchannel designs of Figure 7.

Figure 15 shows that the glass device exhibited efficiencies of up to 57 g/kWh and that the hybrid device yielded efficiencies of up to 85 g/kWh, 30% higher than that for the two glass substance device. The Al/Al_2O_3 device had an efficiency range

similar to that of the hybrid device, but produced O_3 concentrations 2-3 times higher than those for the hybrid devices.

4.2. Ozone Reactor Characteristics of 12 Channel Al/Al_2O_3 Arrays

Figure 16 shows the ozone production rate for the Al/Al_2O_3 device in terms of discharge power for a range of oxygen flows from 0.1 slm to 2.5 slm. This figure shows that for flow rates of 0.5 slm and above, saturation of the ozone production rate was not detected. However, for flow rates below 0.5 slm, the ozone production rate appears to taper off as the discharge power is increased past ~1.2 W. This implies that each individual channel requires an oxygen flow rate of at least .033 slm of oxygen flow in order to avoid saturation.

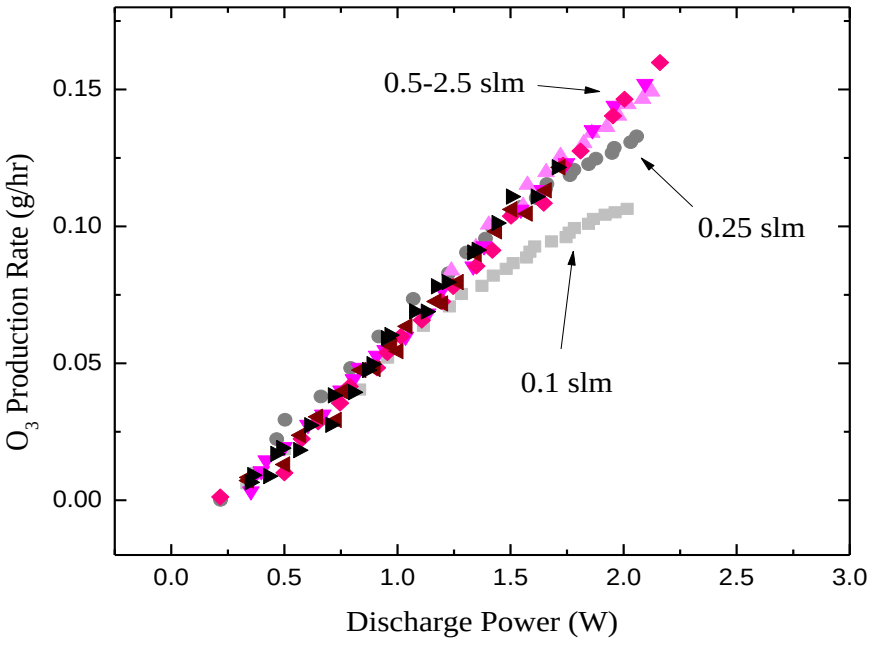

Figure 16. Dependence of the ozone production rate on discharge power for an array of 12 microchannels. Oxygen flow rates of at least 0.5 slm are necessary to maintain the linear rise in production rate for P>1.2W

Figure 17 shows the ozone production rate for an array of 12 microchannels versus discharge power for pure oxygen and a dry air mixture. From this figure, it is clear that a greater ozone production rate can be achieved with pure oxygen than with dry air, and the production rate with oxygen is nearly twice that of air for a discharge power of ~1.9W.

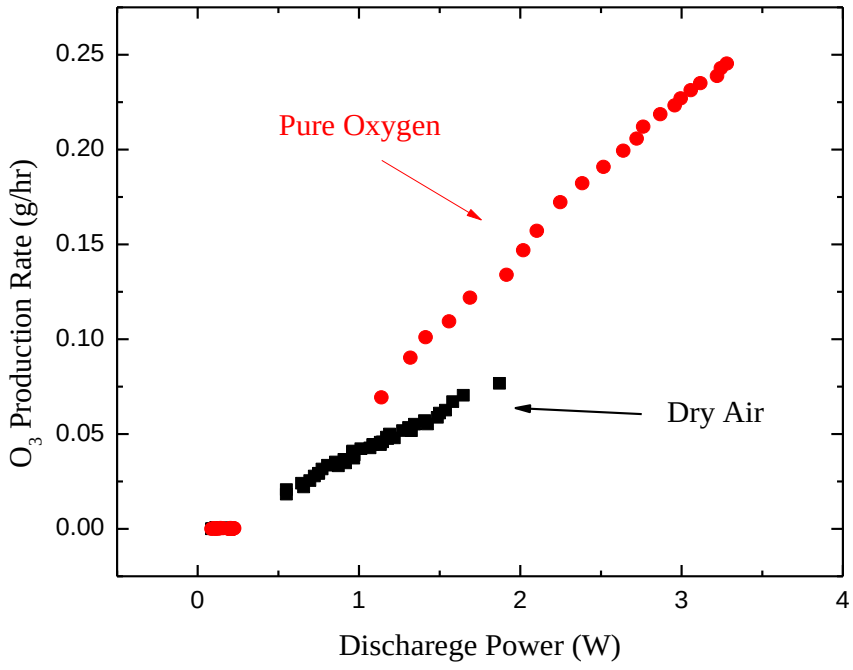

Figure 17 Comparison of the ozone production rates for O_2 or dry air as the feedstock gas. The slope of the solid line corresponds to h = 85 g/kWh whereas the data for air yield an efficiency of 40 g/kWh.

Figure 18 shows that 1 % v/v of nitrogen gas added to the feedstock gas flow stream appears to increase efficiency by as much as 15%. A possible reason for this phenomenon is related to the mechanisms by which the ozone molecule is produced in the discharge. The addition of nitrogen, in particular, appears to provide the third

body required by Fig. 4(b) for the generation of O_3. Note that the influence of N_2 is particularly noticeable at high ozone concentration which is precisely what one would expect on the basis of the three body formation mechanism for ozone.

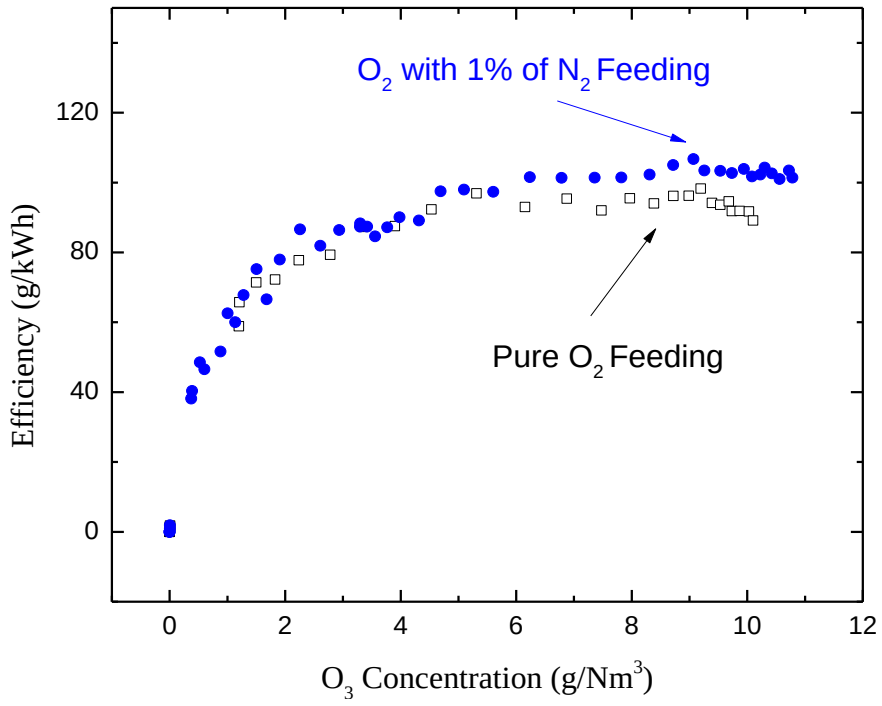

Figure 18. Variation of the O_3 generation efficiency η with the ozone concentration (C) for an O_2 gas flow rate of 0.5 slm. Data are given for the adding 1% of nitrogen gas into pure oxygen gas and only feeding pure oxygen gas

4.3. Extended and Dual-Sided Arrays of Al/Al_2O_3 Linear Channels

Two different geometries have been investigated for the purpose of increasing the number of channels in these microplasma reactors. Figure 19 illustrates these two devices geometries. The linear structure packs more channels on one side of the device, while the stack structure includes channels on both sides. All the devices were fabricated with the same number of channels (24).

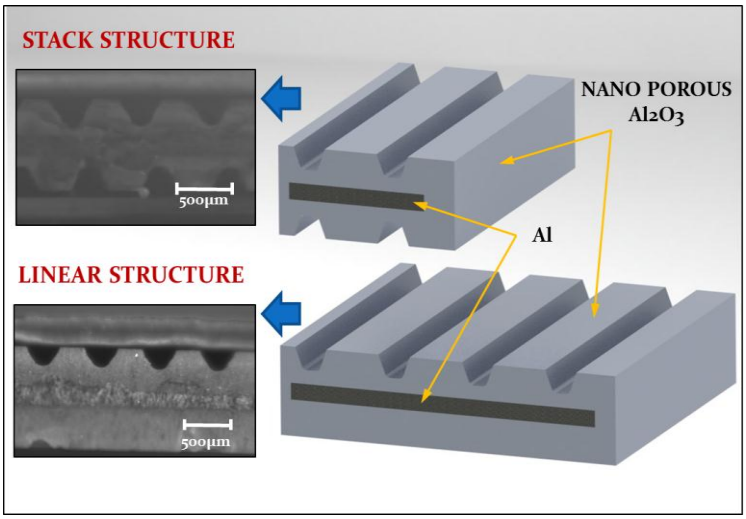

Figure 19. Illustrations of a single, planar array (Bottom) of Al/Al_2O_3 microplasma channels, and (Top) its double-sided counterpart.

Figure 20 shows the measured ozone production rates for arrays of a differing number of channels devices versus discharge power. This figure shows that the rate of ozone production is linearly proportional to the number of channels for both geometries

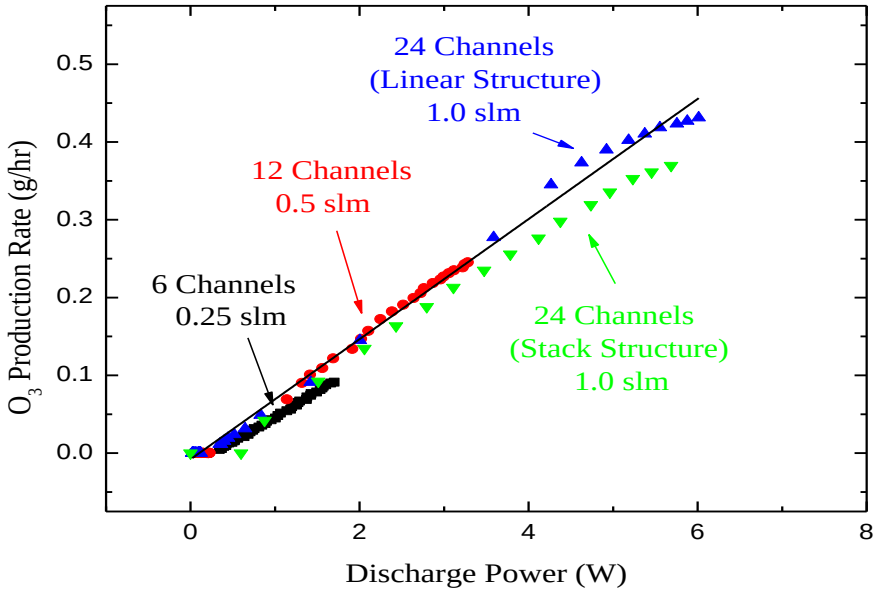

Figure 20. Linear variation of the ozone production rate with discharge power for several Al/Al_2O_3 microchannel arrays (6, 12, and 24 channel planar arrays and a 24 channel double-sided array). The solid line represents an O_3 generation efficiency of 81g/kWh.

4.4. Analysis Of The Ozone Formation Efficiency (Aluminum Device)

A numerical simulation has been performed in an effort to better understand the behavior of the Al/Al_2O_3 devices in terms of their performance relative to the maximum theoretical efficiency. Two assumptions were made in these simulations. First, the $(A^3\Sigma_g^+)$ and $(B^3\Sigma_u^-)$ states of the oxygen molecule in Fig. 4 are assumed to be the only electronic excited states of the molecule that participate as intermediates in the dissociation process. Another assumption is that all excited atoms form ozone in a collision with an oxygen molecule. Each of the rate coefficients, k_1 and k, are a function of electric field strength normalized to N (i.e., E/N). The fundamental equation in the simulation is:

$$k = \int f(\varepsilon) \cdot \left(\frac{\varepsilon}{m_e}\right)^{\frac{1}{2}} \cdot \sigma(\varepsilon)\, d\varepsilon \quad cm^3 s^{-1} . \tag{4.3}$$

In Eq. (4.3), ε is the electron energy, $f(\varepsilon)$ is a distribution function which is a function of electron temperature, and $\sigma(\varepsilon)$ is the cross-section for the process in question which is also a function of E/N. The cross-section for the two rate coefficients used in these simulations can be found in Ref. 15 and Fig. 21.

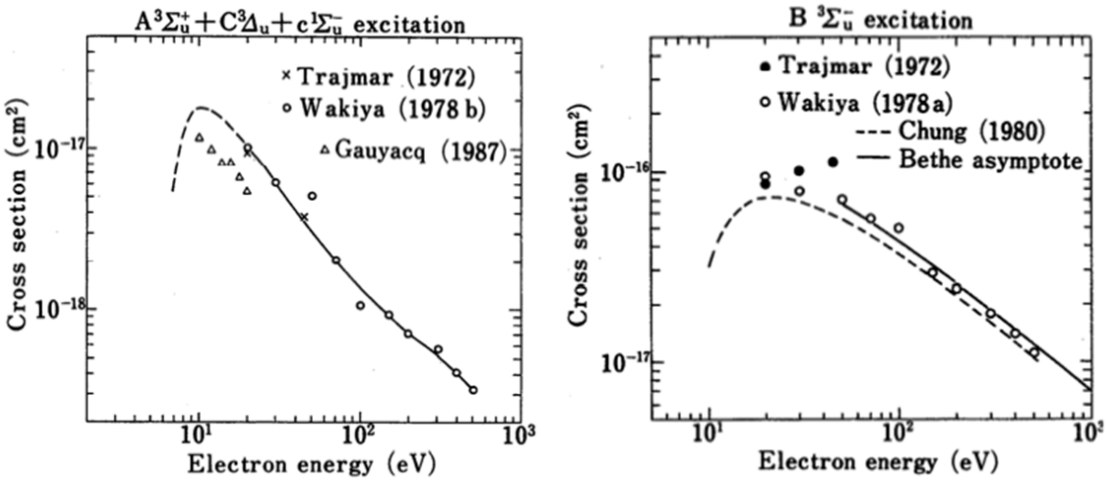

Figure 21 Dependence on electron energy for the cross-section associated with electron impact excitation of the A and B states of oxygen. [15]

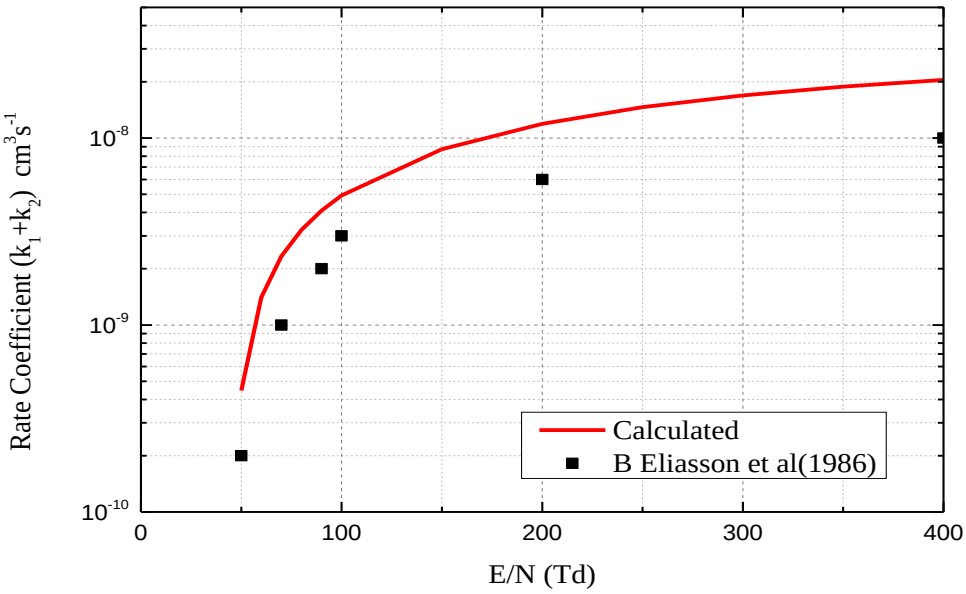

Figure 22. Total rate coefficient for the two dissociation reactions included in this model. The calculated curve is shown in red, and experimental values are in black. [14]

The total rate coefficient for the two electronic dissociation reactions is the sum of k_1 and k_2. For E/N = 200 and 300 Td, the coefficient is found to be 1.2×10^{-8} and 1.8

$\times 10^{-8}$ cm^3s^{-1}, respectively, which are 20% higher than the experimental data of Ref. 14. However, other values reported in the literature have ranged from 2×10^{-10} to 1 $\times 10^{-8}$ cm^3s^{-1} [16,17]. The effiency for generating ozone can be estimated on the basis of the following equations:

$$n_{o_{radical}} = \frac{2(k_1+k_2)N}{v_{drift}} \tag{4.4}$$

$$and\ ,\ \Delta E_{total} = \frac{eE}{\kappa} \tag{4.5}$$

$$so,\ \eta_{Theoretic} = \frac{O_3\ Production}{Discharge\ Power} \propto \frac{n_{o_{radical}}}{\Delta E_{total}} = \kappa \frac{2(k_1+k_2)}{e\, v_{drift}\,(\frac{E}{N})}\,. \tag{4.6}$$

In these equations, κ is the fraction of the total energy gained from electron, ΔE_{total} is the total energy gained by an electron and v_{drift} is the drift velocity. From the notation in Ref. 14, estimated κ to be 0.5 because the silent discharge is considered to be developed to the stage of the streamer discharge, where electrons and positive ions are produced evenly along the discharge columns [18]. The theoretical efficiency is defined as the amount of ozone generated for a given discharge power. For the work in this thesis, the fraction κ is 0.2 since side reactions to those of Fig. 4 have been neglected. In other work reported in the literature, values of 0.2 (20%) [9] and 0.55(55%) [14] were adopted.

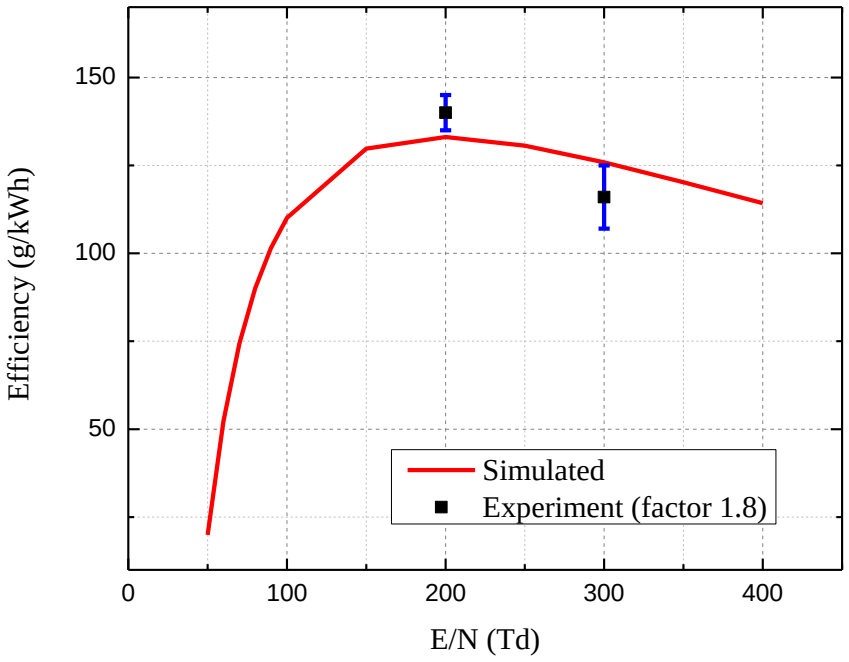

Figure 23 Comparison of simulated and experimental results

Figure 23 presents a comparison of the simulated and experimental efficiencies. Notice that the simulated curve predicts that E/N is approximately 200 Td for maximum efficiency. After this point, the efficiency drops linearly. One possible reason for this behavior is that the efficiency values are inversely propotional to E/N and the rate constant is satuated above 200 Td. As the graph shows, the theoretical efficiency result is roughly a factor of 1.8 lower than the experimental data, but the general tendency for the efficiency versus electric field strength (E/N) is predicted correctly by the calculations. Furthermore, other properties of the plasma, such as T_e, T_g and n_e, have been calculated with the following equations:

$$T_e = T_g + \frac{2}{3k_B} \cdot \left(\frac{2m_e}{M_g}\right)^{-1} \cdot \left\{\frac{q^2}{m_e {k_m}^2}\left(\frac{E}{N}\right)^2\right\} \approx 4.5\ eV \quad (4.7)$$

$$T_g = \frac{1}{d}\int_0^d T(x)dx = \frac{W_{pd}}{3k}d + T_{wall} \approx T_{wall} \approx 300\ K, \quad (4.8)$$

$$and\ \ n_e = J \cdot m_e \cdot \frac{k_{mon}}{q^2 \frac{E}{N}} \approx 9.5\ \times 10^{12}\ cm^{-3}. \quad (4.9)$$

In Eqns. (4.7-4.9), d is the electrode gap, W_{pd} is the discharge power density, k is thermal conductivity, T_{wall} is the wall temperature of the device, and J is the current density. The constants adopted for the solution of these Equations are given in Table I below.

m_e(kg)	M_q(kg)	q(C)	k_m(cm^{3}s^{-1})	k_B(J/K)
9.11×10^{-31}	2.66×10^{-26}	1.60×10^{-19}	4×10^{-8}	1.38×10^{-23}

E/N(Td)	Current(mA)	Area(cm^2)	J(mA/cm^2)	T_g(K)
200	4	0.3	13.3	300

Table 1. Assumed values of constants.

The equations above were solved, subject to the following assumptions:

1. The electron temperature was not included with the loss terms. Also, the only E/N values considered were 200 Td and 300 Td.
2. The discharge power density and thermal conductivity terms were ignored for the calculation of gas temperature, since the thermal conductivity for the aluminum-alumina materials in the experiments is ~40 W/m·K, so the device absorbs most of the dissipated heat.
3. The gas temperature and the current density were measured from the experimental results.

From Ref. 9, T_e ranges up to 5 eV, T_g is approximately 320 K and n_e can be as large as 1×10^{14} cm^{-3}. These values cannot be compared directly with the experimental data, but they do provide a valuable check in that they are typical of the parameters of many microplasma devices.

Chapter 5 – Conclusion

A novel method of generating ozone, based on arrays of microchannel plasmas operating in oxygen or air, has been investigated here. These arrays, fabricated in nanoporous alumina and aluminum substances, demonstrate that competitive O_3 generation efficiencies and concentrations (104 g/kWh and 17 g/Nm^3, respectively) can be realized with this technology. The reactors demonstrated here offer considerably reduced weight and volume (for a given g/hr production capacity), relative to conventional DBD technology, in a robust materials system and structure. An additional benefit of machining microchannels in nanoporous alumina is the deserved ten-fold enhancement of ozone generation efficiency in Al_2O_3 pellet-packed reactors [8]. Although limited scaling of the reactor size and throughput have been demonstrated here, the data presented in the last section correspond to maximum O_3 yields of ~ 2.4 g per ml of reaction (active plasma) volume.

Also, experiments with expanded arrays of linear channels were reported in which planar and dual-sided arrays of 24 channels have been fabricated and tested successfully. Calculations based on the data presented earlier indicate that “massively parallel” ozone generation in arrays of thousands of microchannels has the potential to surpass the efficiency of large conventional DBD systems and to do so in reactors at least an order of magnitude smaller in weight and volume. Reducing the size and complexity of conventional ozone generator systems is expected to remove a significant barrier to the broad adoption of the disinfection of municipal water supplies by ozonation.

Future works

Ozone production in the micro channel plasma device has been introduced and investigated using pure oxygen and dry air. The device can be optimized to improve energy efficiency; therefore, further research and analysis are needed for micro plasma ozone devices to consider different geometries considering heat transfer and gas flow dynamics. There also needs to be more focus on electrical elements to improve efficiency such as power system to drive the plasma and optimization of the electric field for confining plasma.

References

1. Cho, J. H., M. H. Kim, S. J. Park, and J. G. Eden. "Arrays of Microplasma Jets Generated by Double Parabolic Microcavities in an Hourglass Configuration.". *IEEE Trans. Plasma Sci.*, 39, no. 11,p. 2376-77, 2011.
2. Eden, J. G., and S. J. Park. "Microcavity Plasma Devices and Arrays: A New Realm of Plasma Physics and Photonic Applications." *Plasma Physics and Controlled Fusion* 47, p. B83-B92, 2005.
3. Sung, S. H., I. C. Hwang, S. J. Park, and J. G. Eden. "Interchannel Optical Coupling within Arrays of Linear Microplasmas Generated in 25-200 Mu M Wide Glass Channels." *Applied Physics Letters* 97, no. 23, 2010.
4. Chen, J. J., H. H. Yeh, and I. C. Tseng. "Effect of Ozone and Permanganate on Algae Coagulation Removal - Pilot and Bench Scale Tests.". *Chemosphere* 74, no. 6 , p. 840-46, 2009.
5. Huang, F. M., L. Chen, H. L. Wang, and Z. C. Yan. "Analysis of the Degradation Mechanism of Methylene Blue by Atmospheric Pressure Dielectric Barrier Discharge Plasma." . *Chemical Engineering Journal* 162, no. 1,p. 250-56, 2010.
6. de Velasquez, M. T. O., M. N. Rojas-Valencia, and A. Ayala. "Wastewater Disinfection Using Ozone to Remove Free-Living, Highly Pathogenic Bacteria and Amoebae.".*Ozone-Science & Engineering* 30, no. 5, p. 367-75, 2008.

7. Komanapalli, I. R., and B. H. S. Lau. "Ozone-Induced Damage of Escherichia Coli K-12." . *Applied Microbiology and Biotechnology* 46, no. 5-6,p. 610-14, 1996.
8. Chen, H. L., H. M. Lee, and M. B. Chang. "Enhancement of Energy Yield for Ozone Production Via Packed-Bed Reactors.". *Ozone-Science & Engineering* 28, no. 2 , p. 111-18, 2006.
9. Eliasson, B., M. Hirth, and U. Kogelschatz. "Ozone Synthesis from Oxygen in Dielectric Barrier Discharges.". *Journal of Physics D-Applied Physics* 20, no. 11, p. 1421-37,1987.
10. Jodzis, S., T. Smolinski, and P. Sowka. "Ozone Synthesis under Surface Discharges in Oxygen: Application of a Concentric Actuator.". *Ieee Transactions on Plasma Science* 39, no. 4, p. 1055-60, 2011.
11. Kogelschatz, U., B. Eliasson, and M. Hirth. "Ozone Generation from Oxygen and Air - Discharge Physics and Reaction-Mechanisms.". *Ozone-Science & Engineering* 10, no. 4, p. 367-77, 1988.
12. Yamatake, A., K. Yasuoka, and S. Ishii. "Ozone Generation by a Dc Driven Micro-Hollow Cathode Discharge in Nitrogen-Mixed Oxygen Flow.". *Japanese Journal of Applied Physics Part 1-Regular Papers Short Notes & Review Papers* 43, no. 9A, p. 6381-84, 2004.
13. Zhu, W. D., and J. L. Lopez. "A Dc Non-Thermal Atmospheric-Pressure Plasma Microjet.". *Plasma Sources Science & Technology* 21, no. 3, 2012.
14. J Kitayama and M Kuzumoto. "Analysis of ozone generation from air in silent discharge." *Journal of Physics D: Applied Physics*, 32 3032, 1999.

15. Itikawa, Y., A. Ichimura, K. Onda, K. Sakimoto, K. Takayanagi, Y. Hatano, M. Hayashi, H. Nishimura, and S. Tsurubuchi. "Cross-Sections for Collisions of Electrons and Photons with Oxygen Molecules.". *Journal of Physical and Chemical Reference Data* 18, no. 1,p. 23-42, 1989.

16. Brandenburg, R. "Diffuse Barrier Discharges in Nitrogen with Small Admixtures of Oxygen: Discharge Mechanism and Transition to the Filamentary Regime." *JOURNAL OF PHYSICS D: APPLIED PHYSICS* , P. 2187–97, 2005.

17. M. Cacciatore, M. Capitelli and M. Dilonardo. "Non Equilibrium Vibrational Population and Dissociation Rates of Oxygen in Electrical Discharges: The Role of Atoms and of the Recombination Process." *General & Introductory Physics* , p. 279-299, 1978.

18. Yagi, S, and M Tanaka. "Mechanism of Ozone Generation in Air-Fed Ozonisers." *Journal of Physics D: Applied Physics* 12, no. 9, p. 1509, 1979.